Deciphering the Double-Layer Structure and Dynamics on a Model Li(x)MoO(3) Interface by Advanced Electrogravimetric Analysis.

Ezzoubair Bendadesse, Anatolii V. Morozov, Artem M. Abakumov, Hubert Perrot, Jean-Marie Tarascon, Ozlem Sel

Deciphering the double layer structure and dynamics on a model Li_xMoO_3 interface by advanced electrogravimetric analysis

Ezzoubair Bendadesse[a,b,c], Anatolii V. Morozov[d], Artem M. Abakumov[d], Hubert Perrot[c], Jean-Marie Tarascon[a,b,*], Ozlem Sel [a,b,*]

[a] Chimie du Solide et de l'Energie, UMR 8260, Collège de France, 11 Place Marcelin Berthelot, 75231 Paris Cedex 05, France

[b] Réseau sur le Stockage Electrochimique de l'Energie (RS2E), CNRS FR 3459, 33 Rue Saint Leu, 80039 Amiens Cedex, France

[c] Sorbonne Université, CNRS, Laboratoire Interfaces et Systèmes Electrochimiques, LISE, UMR 8235, 4 Place Jussieu, 75005 Paris, France

[d] Center for Energy Science and Technology, Skolkovo Institute of Science and Technology, Nobel str. 3, 121205 Moscow, Russia

Corresponding authors:

jean-marie.tarascon@college-de-france.fr

ozlem.sel@college-de-france.fr

Abstract:

A major feature of the Electrolyte/Electrode Interface (EEI) that affects charge storage in Lithium-ion batteries is the electrical double layer (EDL), but most of the available experimental approaches for probing its structuration have limitations due to electrical field and redox reactions disturbances, hence explaining why it is frequently overlooked. Herein we show that this is no longer true by using an advanced Electrochemical Quartz Crystal Microbalance (EQCM) based method in the form of *ac*-electrogravimetry. For proof of concept, we studied the effect of various solvent/salt combinations, differing in their dipole moment and size/weight respectively, on the structure of the EDL forming at the EEI of Li_xMoO_3. We show that a significant amount of solvated lithium ions and anions contribute to charge compensation at the interface and by varying the nature of the solvents (cyclic *vs* non cyclic), we provide a solid experimental proof of the direct relationship between the ions' solvation and solvent polarity. Moreover, we demonstrated a disappearance of the anionic motion in the less polar solvent (DMC) most likely due to plausible formation of contact ion pairs and agglomerates at

the EDL level. Altogether, *ac*-electrogravimetry, when combined to classical EQCM, stands as an elegant and powerful method to experimentally assess the chemical structure and dynamics of the electrical double layer. We hope that the community will start to adopt it to better engineer interfaces of electrochemical energy storage devices.

Keywords: Electrochemical energy storage, electrode/electrolyte interface, electrical double layer, EQCM, Li_xMoO_3

Rechargeable M-ion batteries (M = Li, Na, K, Mg…) and electrical double layer capacitors (EDLCs), also called supercapacitors, have been playing an important role in energy storage technologies due to their efficiency and flexibility for providing on-demand the appropriate amount of energy dictated by various applications.[1–3] The choice of a particular energy storage technology depends on several figures of merits such as: power density, energy density, charging speed and cost, with safety remaining the overriding factor for most applications. Such figure-of-merit is determined by the synergy between the cell components, namely: electrodes, electrolytes, and separators, but also by the way they interact. The phenomena related to the electrolyte/electrode interface (EEI) are of paramount importance to battery researchers, as they often play a crucial role in the performance of the cells. One of these EEI phenomena is the ubiquitous electrical double layer (EDL) forming at the electrode/electrolyte interface that is a common aspect of EDLCs and batteries. It consists in a specific structuration of the electrolyte's charge carrier at the oppositely charged electrode interface, that mainly controls charge transfer.[4]

The ion-hopping or vehicle-like transport of lithium ions from the bulk of the electrolyte to the EEI has been described in the literature.[5] When the cation reaches the EDL, it goes through a series of processes that include desolvation, ionic transport (*via* the Solid Electrolyte Interface (SEI) or parallel to the electrode surface) and charge transfer, with one or a combination of these processes acting as the rate limiting factor for ion insertion into the host material.[6,7] Given the intricacy and the interplay between these processes, EDL has long been a complex concept to be mastered by the electrochemical energy storage community in spite of the numerous experimental and theoretical studies dealing with the effect of EDL on the Li-ion battery performance. More efforts are required for describing the EDL behavior, its chemical content and structuration, and it's dynamic during battery charge/discharge.

At the experimental level, great progress has been made over the last two decades in developing *operando techniques* to determine the exact molecular structure of the EDL. Among them are synchrotron-based X-ray surface diffraction and vibrational spectroscopy methods,[8] enlisting Surface Enhanced Raman Spectroscopy (SERS)[9], Tip Enhanced Raman Spectroscopy (TERS)[10], and Infrared Reflection Spectroscopy (IRAS)[11], as well as X-ray photoelectron spectroscopy (XPS)[12,13] and Atomic Force Microscopy (AFM)[14,15]. However, common to all of these techniques is their complex quantification that is frequently subject to controversies, hence explaining their use with other quantitative methods such as Online Electrochemical Mass Spectroscopy (OEMS) and Electrochemical Quartz Crystal Microbalance (EQCM).[16]

Over the last decade EQCM has become a tool of choice for studying EEI-related phenomena in energy storage materials,[17,18] with the feasibility to be a pertinent experimental technique for EDL investigation because the Debye length, which characterizes the "thickness" of the EDL, falls within the penetration depth of the acoustic shear wave emanating from the resonator.[19,20] This technique is nowadays employed to monitor gravimetric variations down to the nanogram scale, but also as a probe[21,22] to characterize the mechanical properties of the SEI as well as to accurately assess the micromechanical stability of the porous structure of battery electrode materials. Along that line, our group recently reported the evolution of the Li^+ solvation shell during the removal-uptake of Li^+ for $LiFePO_4$ in either aqueous or organic media[23] with a generalization of the same methodology to K-ion battery electrode.[24]

Herein, we provide a systematic approach to study interfacial phenomena by pushing the present EQCM based techniques to their limits. These techniques enlist classical EQCM-R which monitors both frequency (Δf) and motional resistance (ΔR_m) changes and the less known so-called *ac*-electrogravimetry which couples electrochemical impedance spectroscopy (EIS) and fast QCM to provide a deeper perspective on the nature and the dynamic of the species transferred at the EDL.[25–28]

As a poof of concept to study the chemical structuring of EDL, we have chosen as model electrode in this work molybdenum (VI) oxide (MoO_3) that is a well know insertion compound that has applications extending from the field of batteries, supercapacitors to the field of electrocatalysis as well as electrochromism. Next, we demonstrated how to use classical and advanced EQCM in the form *ac*-electrogravimetry to first decipher the charge storage mechanism in Li_xMoO_3 by identifying the different species transferring to the EEI. Moreover, we investigated how the EDL's structure

behaves as a function of electrolyte composition, by examining various salt-solvent combinations that differed in the nature of the anions or the polarity and dielectric constant of the selected solvent molecules. Altogether, through this we illustrate the ability of *ac*-electrogravimetry to determine the nature, molar mass and kinetics of the transferred species across the EDL.

Results and discussion

Thin film growth and (electro)chemical characterization

MoO_3 thin films of approximately 110 nm thick (**Fig. 1a**) were deposited *via* chronoamperometry onto the gold electrode of quartz resonators according to a protocol described by Yao *et al.*[29] The resulting film was subsequently heated up to 300 °C for 3h. The X-ray powder pattern (**Fig. 1b**) exhibits only (0k0) peaks of the layered α-MoO_3 structure that is indicative of preferentially oriented nucleation growth. From the broadening of the (020) and (040) Bragg peaks and using the Scherrer equation[30], we could deduce that the films are made of ~33 nm sized crystallites.

Electrochemical tests performed on the 300 °C treated α-MoO_3 thin film in 1M $LiClO_4$ in PC electrolyte shows the presence of an irreversible first lithiation plateau at 2.7 V *vs* Li/Li^+ (**Fig. 1c**) and of an irreversible peak on the first reduction scan in cyclic voltammetry (**Fig. 1d**), alike what has been reported in the literature. In situ X-ray diffraction using an electrochemical cell made of α-MoO_3 powder indicates the initial irreversible formation of the a $Li_{0.25}MoO_3$ phase. Once this phase is formed, the Li insertion/deinsertion proceeds through a reversible solid solution process as reported in the literature.

Moreover, HRTEM images and SAED patterns taken of pristine α-MoO_3 and Li_xMoO_3 confirm that the former adopts a layered orthorhombic structure (S.G. *Pbnm*) with the interlayer distance of ~ 7.0 Å (**Fig. 1f**, left). Noteworthy, the lithiation of α-MoO_3 leads to a well-ordered crystal structure having an interlayer spacing of ~ 7.9 Å (**Fig. 1f**, right) in agreement with the earlier TEM observations.[31] Sharp reflections in the corresponding SAED pattern (inset in **Fig. 1f**, right) witness long-range ordered interlayer spacings without noticeable variation, thus indicating the homogeneous distribution of Li^+ over the volume of the crystallites.

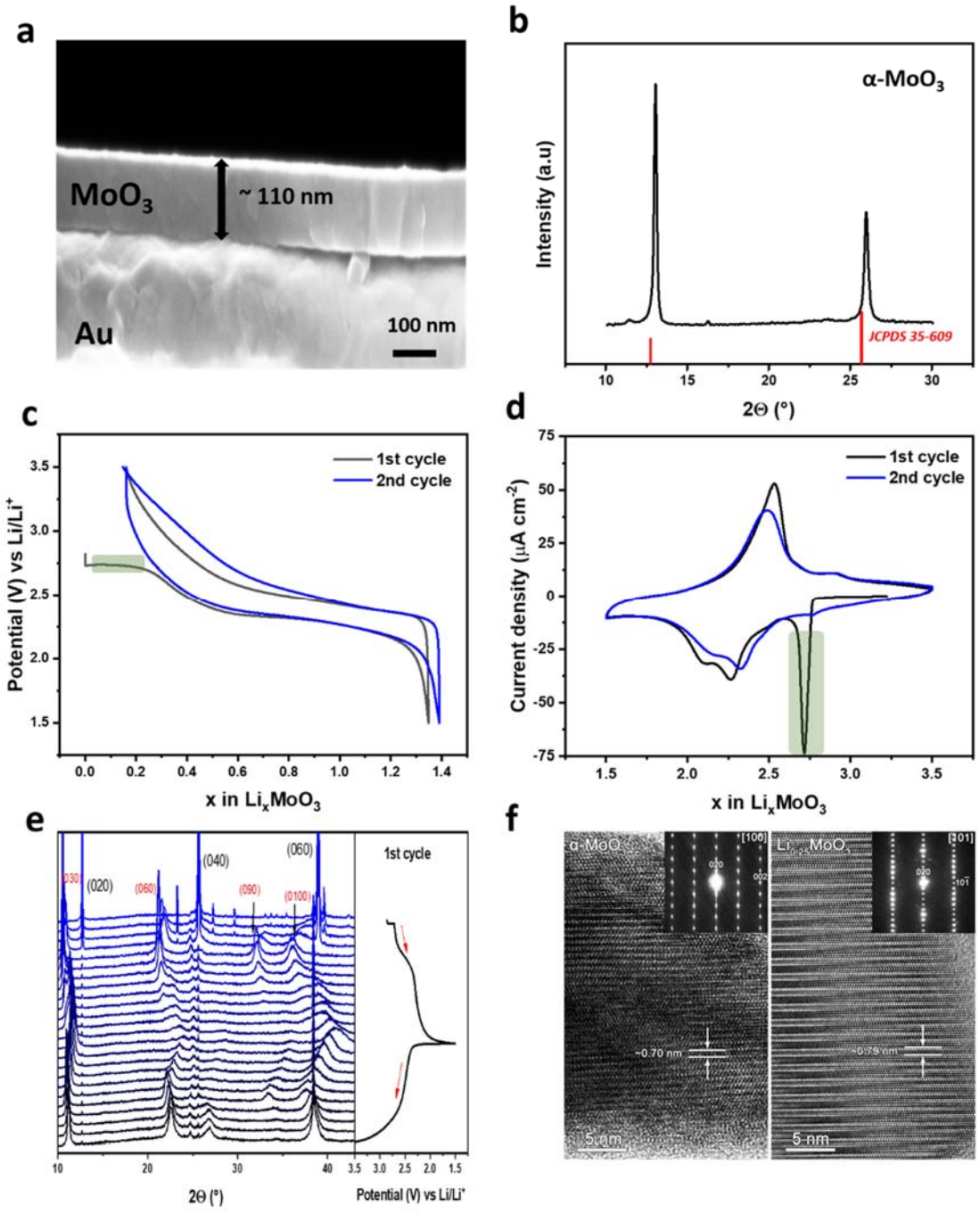

Figure 1. a) FEG-SEM image of MoO_3 thin film electrodeposited onto Au-coated QCM surface and b) XRD pattern of 300 °C treated α-MoO_3 ((0k0) peaks shown here) on the Au-coated QCM (reported α-MoO_3 reference JCPDS 35-609 in red). The panels c) and d) present GCPL and CV profiles, respectively, of α-MoO_3 thin film in 1M $LiClO_4$ in propylene carbonate (PC) (irreversible plateau/peak is highlighted in green). The panel e) is the *in situ* XRD of 1st discharge/charge cycle of α-MoO_3 commercial powder (containing 20 *wt.*% carbon black) cycled under the same conditions as the thin film (lithiated phase is indexed in red). f) HRTEM images of the commercial α-MoO_3 in its pristine (left) and lithiated (right)

state along with the corresponding SAED patterns. Indexes in SAED patterns are given assuming the orthorhombic structure of α-MoO_3 (S.G. *Pbnm*). Values of the interlayer distances for the pristine and lithiated structures are provided in the HRTEM images.

Interface evolution during the first electrochemical cycles monitored by EQCM-R

Fig. 1c and **d** demonstrate that α-MoO_3 undergoes a phase transition during the first electrochemical charge/discharge cycle, in agreement with previous literature reports.[31–33] To grasp further insights into both structural and interfacial phenomena occurring during the first lithiation/delithiation in 1M $LiClO_4$ in PC, EQCM-R analysis that monitors the motional resistance change (ΔR_m) along with the resonator's frequency change (Δf) was performed. It is noteworthy to recall that R_m depends on the roughness of the film deposited on the quartz resonator, viscosity and density changes of the electrolyte at the vicinity of its surface and is affected by excessive mass increase over a short time, as well as structural and/or mechanical changes of the electrode material itself.[34–37] Hence, it is considered as one of the key parameter to interrogate thin film interface during redox processes.

Figure 2a shows that during the electrochemically–driven uptake-removal of Li^+ in α-MoO_3 thin film, there is an initial frequency decrease of about -200Hz (**Fig. 2b**), with a concomitant increase in R_m of about 10Ω (**Fig. S2**) at 2.7V *vs* Li/Li^+ during the cathodic scan. This corresponds to the irreversible phase transition of α-MoO_3 to $Li_{0.25}MoO_3$. Afterwards, R_m increases up to 20% of its original value through the second lithiation peak/plateau located near 2.3V *vs* Li/Li^+ (**Fig. S2**), meanwhile Δf continues to decrease (**Fig. 2b**). The respective increase and decrease of R_m and Δf on the second lithiation can be explained by the continuous lithiation of the framework,[31,33] but also from plausible decomposition of the electrolyte to form an SEI layer onto the surface of Li_xMoO_3.

To decouple the lithiation process from a plausible SEI growth, the lower cut-off potential was limited to 2.3V *vs* Li/Li^+. In presence of α-MoO_3, the irreversible peak on the first reduction at 2.7V *vs* Li/Li^+ appears in both potential windows (**Fig. 2a**). When cycled over the full potential window, α-MoO_3 exhibits an irreversible frequency of ~700Hz (**Fig. 2b**) that decreases through the following cycles (**Fig. S3a**) meaning that the electrolyte continuously degrades over cycling but to a lesser extent. However, when the lower cut-off voltage was limited to 2.3V, the irreversibility is proportional to the frequency drop caused by the first lithiation implying the absence of electrolyte degradation over this potential range (**Fig. 2b**). This is further confirmed by the nearly complete reversibility of the frequency change after the first cycle (2nd cycle is shown in **Fig. S3b**) when the potential window is limited.

Since QCM resonators are coated with an Au electrode, we decided to measure the electrochemical response profile of an Au-coated quartz (free of α-MoO_3 thin film) cycled over the full potential window to distinguish any possible contribution of its catalytic response towards electrolyte decomposition. **Figures 2a** and **b** show that the profile remains featureless down to 1.7V *vs* Li/Li^+, after which a slight cathodic current is recorded (**Fig. 2a**). Noteworthy, there is the frequency drop to -600Hz for the bare Au-coated resonator, suggesting that the electrolyte decomposes irreversibly onto the surface, resulting in an SEI (**Fig. 2b**). As a direct consequence, this implies that the exposed gold surface on the α-MoO_3 thin film catalyzes the degradation of PC into various lithium-containing compounds (carbonates, alkyls and alkoxydes).[38] However, it is worth mentioning that the system seems to stabilize after 20 cycles based on EQCM-R measurements, as conveyed by the low amplitude of ΔR_m (< 20 Ω) and the fully reversible frequency response within a cycle over multiple cycles (**Fig. 2c**). The ΔR_m translates in a low full resonance width change (ΔW) (**Fig. 2c**) calculated following a procedure described in the Supporting Information File (**Equation S1**). After 20 cycles, the condition of the gravimetric sensing is fulfilled as $|\Delta W| << |\Delta f|$[23,39]. Sauerbrey equation (Equation 1) was then employed to convert Δf into Δm (**Fig. 2d**).

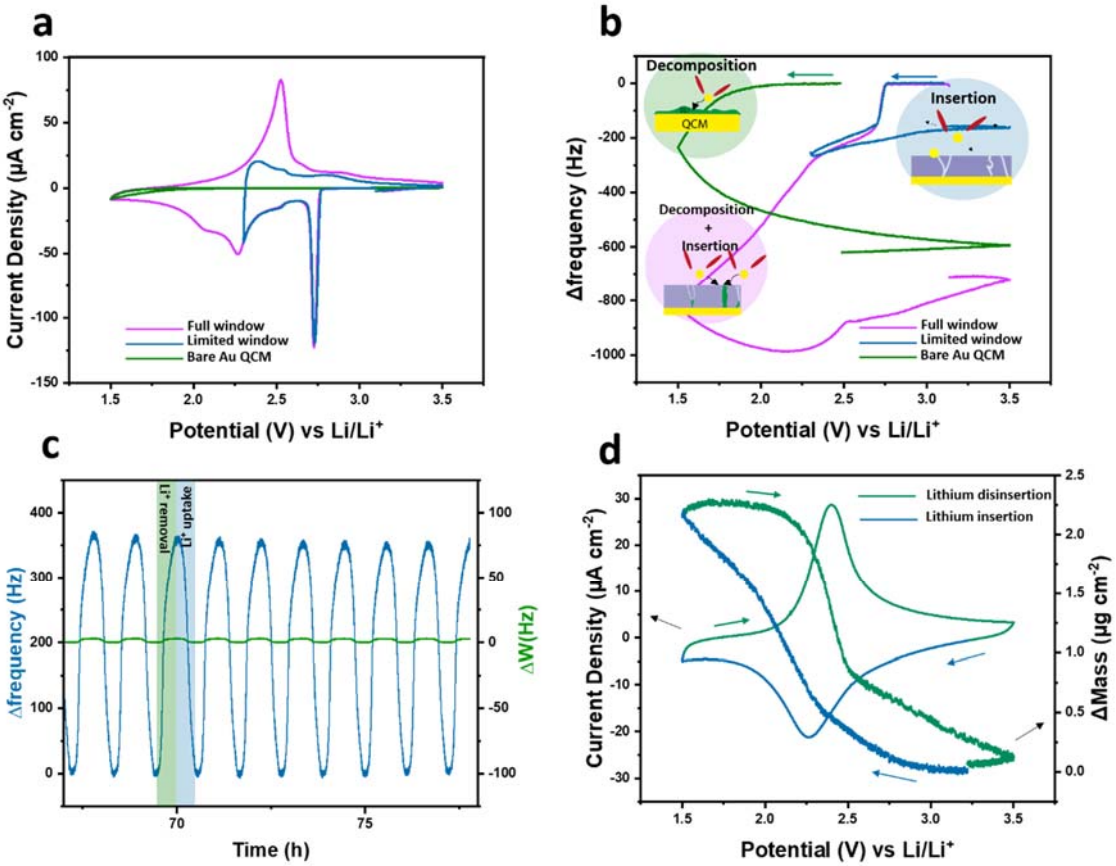

Figure 2. a) CV profiles of α-MoO_3 thin film in 1M $LiClO_4$ in PC in [1.5V; 3.5V *vs* Li/Li^+] and [2.3V; 3.5V *vs* Li/Li^+] measured with two different samples and a bare Au-coated resonator, b) corresponding frequency response of the 1st CV cycles (displayed in panel a). c) Frequency and full resonance width evolution of α-MoO_3 loaded QCM through cycling (20th to 30th cycles are displayed here) and d) 20th CV cycle of α-MoO_3 loaded QCM, the frequency response is translated into mass change using the Sauerbrey equation.[40] All the CV measurements are performed at 1 mV s^{-1}.

Advanced electrogravimetry to the service of EDL probing and charge storage mechanism

Global picture of the interfacial process with EQCM-R. The reversible change in Δm measured during the electrochemical cycling of Li_xMoO_3 in 1M $LiClO_4$ in PC (starting the 20th cycle, **Fig. 2c**) was analyzed to get a global picture of the interfacial processes. To that end the Δm *vs* ΔQ plot is a convenient way towards identifying the species interacting with the electrode material as its slope is proportional to the apparent molar weight (see Experimental part), providing that there is strictly one species participating in the charge compensation process.

Fig. 3a shows the deviation from the slope corresponding to the ideal Li^+ intercalation (estimated from the charge accumulated during reduction). The slope and the resulting average mass per electron value (M.P.E) seem to be in good accordance with Li^+ molar mass in region I but start deviating negatively and positively in regions II and III, respectively. This behavior may suggest the presence of several species interacting with the Li_xMoO_3/electrolyte interface. During reduction, Li^+ inserts into the structure and the molar mass in region I and II is around 7.07 and 6.33 g mol^{-1}, respectively (**Fig. 3b**), these values slightly deviate from $M_w(Li^+)$ = 6.9 g mol^{-1}. When reaching lower potentials, one can notice a third slope of ~19.4 g mol^{-1}, this multiple slope behavior is reversible and has been recorded on the reverse scan, with a smaller value (**Fig. 3c**). No other species besides Li^+ can be justifiably ascribed to the second slope observed in the Δm *vs* ΔQ plot, as the molar masses of anions (ClO_4^-) and the solvent (PC) (99.45 and 102.09 g mol^{-1}, respectively) are ~6 times higher than the value recorded. In a similar manner, we illustrate this discrepancy by comparing the mass measured by our quartz resonator (Δm_{EQCM}) and the mass calculated *via* Faraday's law assuming sole Li^+ intercalation ($\Delta m_{Faraday}$). A clear difference is observed with Δm_{EQCM} being higher than $\Delta m_{Faraday}$ by 0.65 µg cm^{-2} (**Fig. 3d**), calling for a more thorough investigation to determine the true nature of the species transferring to the EEI.

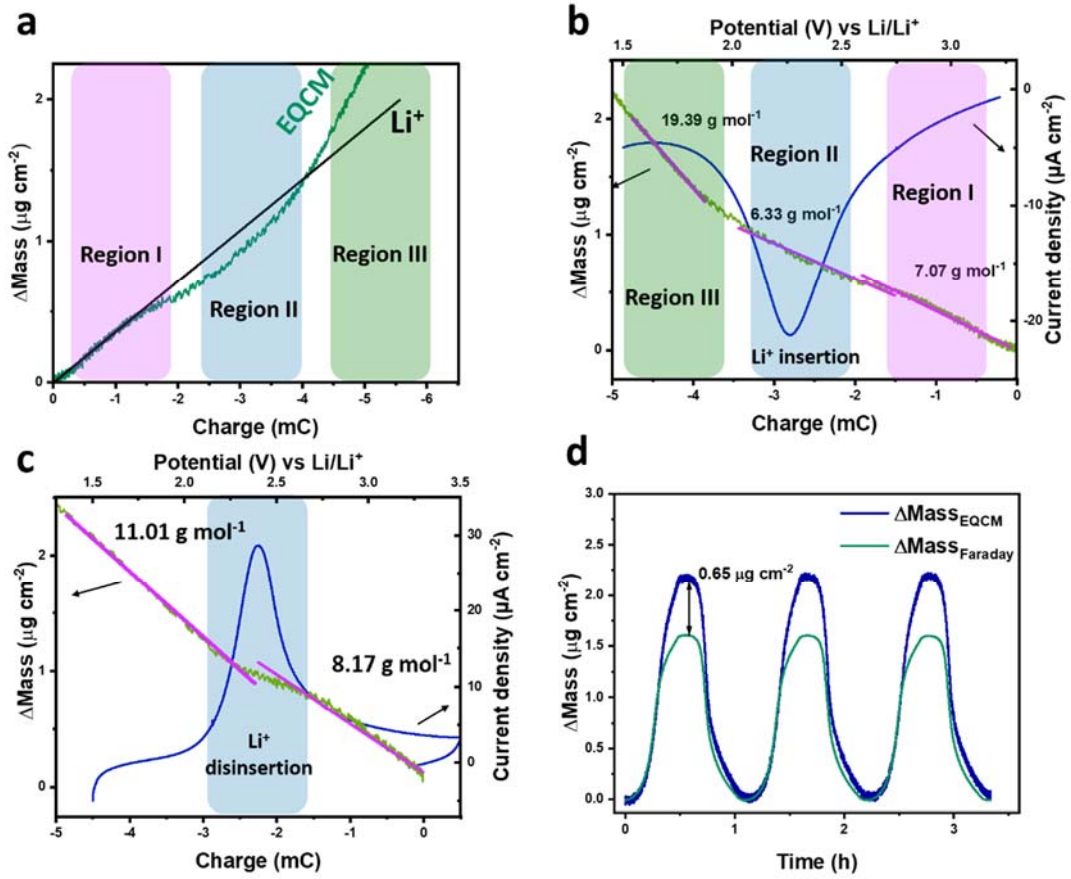

Figure 3. Δm *vs* ΔQ plots of Li_xMoO_3 obtained from the EQCM analysis (Fig. 2a, b) in 1M $LiClO_4$ in PC where a) Δm_{exp} deviation from Δm_{theo} (equivalent to Δm_{EQCM} and $\Delta m_{Faraday}$, respectively) is shown, assuming only Li^+ insertion calculated via Faraday's law (from reduction branch) and |M.P.E.| values through lithiation in b) (the same regions represented in a)) and delithiation in c) (linear fit in purple). Panel d) comparison between Faraday mass calculated by assuming sole Li^+ (dis)insertion and EQCM mass detected by the resonator, shown for 3 consecutive cycles, (cycles 15 to 17). All the CV measurements are performed at 1 mV s^{-1} (previously cycled at 0.5 mV s^{-1} for stabilization).

Deciphering the interfacial process and EDL structuring via ac-electrogravimetry. *Ac*-electrogravimetric measurements were carried out at various stationary potentials, within the highlighted potential region surrounding the faradaic peaks of the CV in **Fig. 3b** and **c**, to which a small potential perturbation was superimposed. In addition to the typical electrochemical impedance ($\Delta E/\Delta I(\omega)$) transfer function (TF) (from which we derive the charge/potential TF $\Delta q/\Delta I(\omega)$), the so-called mass-potential TF ($\Delta m/\Delta E(\omega)$) was acquired in real-time. The latter enables the identification of the nature of species and their dynamics of transfer at electrode/electrolyte interface to be

estimated (Supporting information File for more details[25–28]). Experimental $\Delta m/\Delta E(\omega)$ TF measured at 2.3 V *vs* Li/Li^+ presents two distinct loops. The first relatively small loop appeared in the first quadrant and the second loop expanded over the second and third quadrants (**Fig. 4a**). Alike required in typical EIS measurements, the experimental TFs (mass-potential, charge/potential TFs *etc.*, detailed in Supporting Information) were fitted to extract relevant parameters to decipher the interfacial processes. Several configurations (*e.g.* single ion contribution) for the fitting process have been considered but easily eliminated due to the unsatisfactory fit between the experimental and the theoretical curves, leading to the two most plausible sets: (i) a first one comprising of an anion (ClO_4^-), a cation (Li^+) and free solvent molecules (PC) and (ii) a second set consisting of an anion (ClO_4^-) and two cations (Li^+ and Li^+.n[PC]). To discard one of these hypotheses, the experimental charge/potential TF, $\Delta q/\Delta E(\omega)$ (derived from $\Delta E/\Delta I(\omega)$) (**Fig. S6**) and the $\Delta m/\Delta E(\omega)$ TF (**Fig. 4a**) were fitted using **Equation S17** and **S18**. With the hypothesis (i), it was not possible to find a unique set of parameters, leading to a good fit of experimental TFs (*i.e.*, $\Delta E/\Delta I(\omega)$, $\Delta q/\Delta E(\omega)$, $\Delta m/\Delta E(\omega)$ and partial TFs). In contrast, the hypothesis (ii) which enlists a regulation of three charged species' contribution to the total charge has satisfactorily led to a good fit of the $\Delta q/\Delta E(\omega)$ TF (**Fig. S6**), as well as $\Delta m/\Delta E(\omega)$ TF (**Fig. 4a**), in terms of magnitude and frequencies. The K_i (the kinetics of interfacial transfer) and G_i (the inverse of the transfer resistance, R_{ti}) of these species have been determined, their identification by their molar masses (M_i) has been accomplished through the fitting of the $\Delta m/\Delta E(\omega)$ TF (**Fig. 4a**) by using **Equation S18**. The species are identified as two different cations and an anion which corresponds to bare Li^+ (c1), solvated lithium (Li^+.n[PC] where n=1) (c2) and perchlorates (ClO_4^-) (a), respectively and their kinetics of interfacial transfer follows this order: Ka>Kc1>Kc2. By virtue of the theoretical partial mass/potential TFs (**Equation S19** and **S20**), we could fully secure the three species' contribution into charge compensation process (**Fig. S8**). The *ac*-electrogravimetry measurements at the other potentials show that the three charged species' contribution persists, except slight changes in the solvation number of the cation 2, Li^+.n[PC], with $0.7 \leq n \leq 1$.

Altogether, EQCM results in **Fig. 3** revealed a global cationic response, therefore finding an anion contribution is surprising. The perchlorates detected by *ac*-electrogravimetry have an opposite direction to Li^+ interfacial flux (desorption of ClO_4^- during Li-ion species insertion and *vice versa*) and present faster kinetics, such behavior has already been reported in nano-sized Li-rich compounds[41], where PF_6^- and ClO_4^- electro-adsorption/desorption occurs in the opposite direction to Li^+ (de)insertion, as supported by surface X-ray absorption spectroscopy (XAS) and TEM analyses.

Electroadsorption of ions on the surface is also referred to as specific adsorption. It occurs in the Inner Helmholtz Plane (IHP) and is accompanied by either partial or total charge transfer and involves chemical bonding between the surface and the ion.[42] In the present case, the fast ClO_4^- species interaction with the electrode can be described as * + ClO_4^- + δe^- ⇔ *-$ClO_4^{(1-\delta)-}$, where * represents a free electroadsorption site on Li_xMoO_3 surface and δ the amount of partial charge transferred per ClO_4^-. The anion charge carried by the oxygen is then reduced and oxidized following discharge and charge, respectively.[41]

It is clear from **Fig.4b** that the major contributor to charge compensation is bare Li^+ cations, their contribution to the total charge was calculated to be ~ 92% (calculated from **Equation S15** and **17**). Li^+ cations are inserted into the α-MoO_3 framework as proven by the faradic nature of the CV profile and the *in-situ* XRD data of the second cycle showing clear solid solution growth behavior (**Fig. S7**).

Solvated lithium was found to be the second largest contributor to charge compensation, accounting for 5.5% of the total charge accumulated, while ClO_4^- made up the remaining 2.5% (**Fig. 4b**) (these values were adequate with surface concentration of electroactive sites calculated from the electrochemically active surface area using equations S21 and S22). Indeed, contribution of each species into mass change is governed by their contribution in the total charge accumulation, but also by their molar mass. Thus, despite their low contributions into charge, solvated Li^+ and ClO_4^- make up to 38% and 14% of the total mass exchanged, respectively (**Fig. 4b** and **4d** left panel).

Surprisingly, the slowest species to be transferred to the interface is the solvated lithium Li^+.n[PC] which is nearly one order of magnitude slower than its bare counterpart (**Fig. 4c**). Such slow kinetics can lead to envision intercalation of Li^+ with a part of their solvation shell which is physically plausible from a structural standpoint.[33] However, in this case, (quasi)specific adsorption of solvated Li^+ is preferred because the HRTEM results show an expansion in the interlayer (compared with α-MoO_3) that is not sufficient to justify solvent insertion (0.9 Å) (**Fig. 1f**). This confirms the co-habitation of solvated Li^+ along anions in the IHP, and a mediation of the adsorption process by anionic species could be considered as a quasi-specific adsorption of solvated lithium species.[42]

Finally, the origin of the discrepancy between the $\Delta m_{Faraday}$ and Δm_{EQCM} witnessed in **Fig. 3d** can be clarified with the set of species revealed by the *ac*-electrogravimetry. The anionic/cationic repartition attained by this tool (calculated from **Equation S15**, **Fig. 4b**) can be implemented into Faraday's law as charge fractions, $(x_{L_i^+}, x_{L_i^+.[PC]_n} and\ x_{ClO_4^-})$ in the following manner:

$$\Delta m_{ac-EQCM} = \frac{\Delta Q}{n * F}\left[(x_{L_i^+} \times M_{L_i}) + (x_{L_i^+.[PC]_n} \times M_{L_i^+.[PC]_n}) - (x_{ClO_4^-} \times M_{ClO_4^-})\right] \quad \text{Equation 1}$$

We obtain a near perfect agreement of the re-calculated $\Delta m_{ac\text{-electrogravimetry}}$ with the measured Δm_{EQCM} (**Fig. 4d**), thus confirming the proposed ionic repartition in the charge-compensation process. Then, the discrepancy in **Fig. 3d** is due to neglecting the interfacial phenomena and attributing the whole process to the bare Li^+ ions' insertion. This finding further highlights the complementarity of *ac*-electrogravimetry to classical EQCM in providing a deeper level of understanding of the EEI processes.

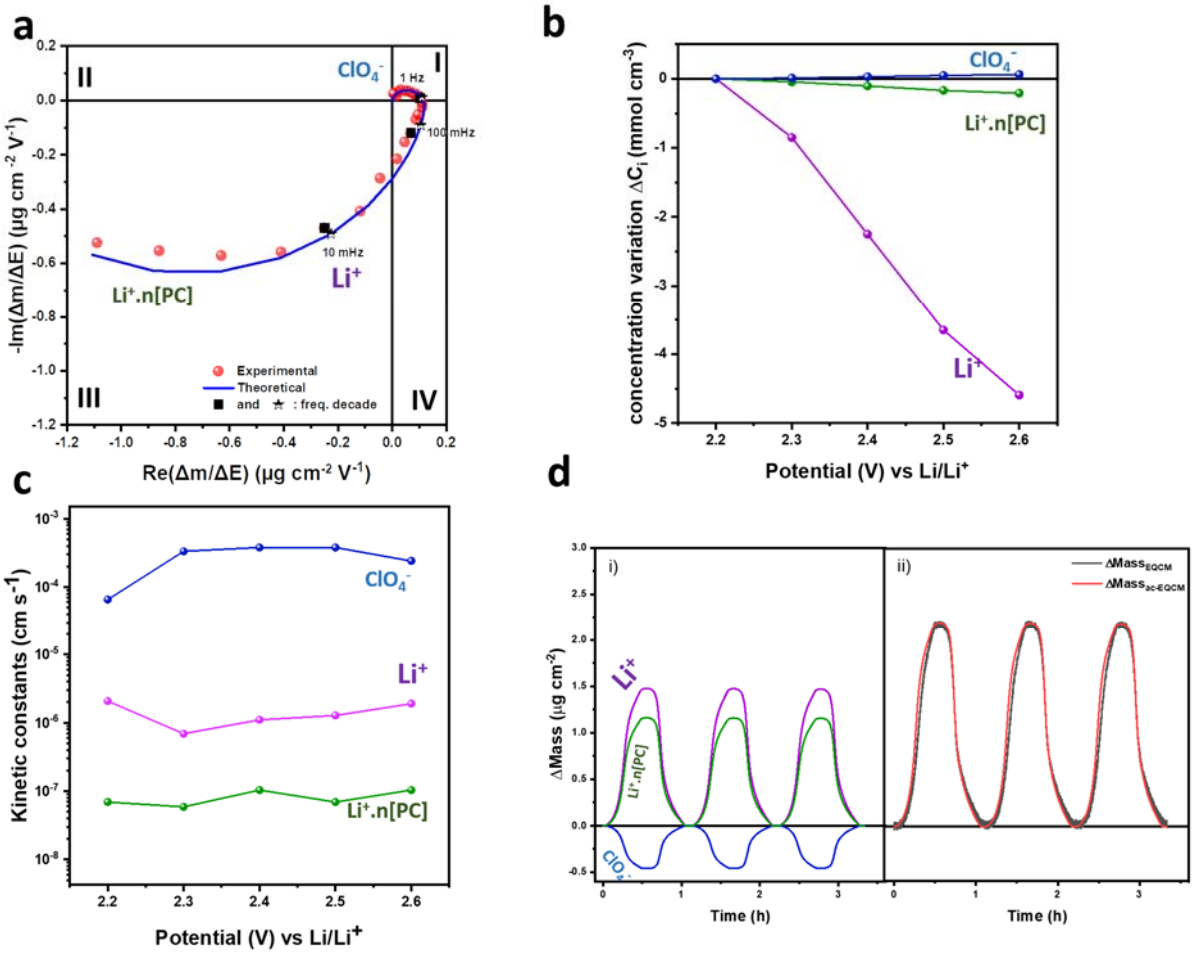

Figure 4. a) Ac-electrogravimetry response of Li_xMoO_3 thin film in 1M $LiClO_4$ in PC electrolyte at 2.3 V vs Li/Li^+, where experimental $\Delta m/\Delta E(\omega)$ transfer function (TF) was fitted with the contribution of three species, i (i=Li^+, Li^+.n[PC] with n = 1, and ClO_4^-) transferred at the EEI, b) concentration variation of the species (ΔC_i) estimated from Equation S13-15, c) kinetic of interfacial transfer (K_i) of the different species over the probed potential window and d) the left panel (i) is the contribution of each species into the total Δm considering their flux directions, estimated *via ac*-electrogravimerty. Using the mass proportions of each species portrayed in panel

(i), total $\Delta m_{ac\text{-}electrogravimetry}$ is calculated and presented in red, right panel, ii. Panel (ii) on right compares the $\Delta m_{ac\text{-}electrogravimetry}$ with Δm_{EQCM}. Fitting parameters of the *ac*-electrogravimetry data at 2.3 V *vs* Li/Li^+ are shown in **Table S1**.

How the interfacial process and EDL structuration differ as a function of electrolyte composition?

To substantiate the above findings observed in 1M $LiClO_4$ in PC and to investigate the effect of electrolyte composition on the EDL structuration, we have modified the salts (anion species) and the solvent itself by changing its molecular weight and polarity. Firstly to confirm the presence of anions as part of the charge compensation process we replace the ClO_4^- anion ($M_{w(ClO4^-)}$: 99 g mol^{-1}) in PC by an anion having a threefold greater mass such as bis(trifluoromethane)sulfonimide ($TFSI^-$; $M_{w(TFSI^-)}$: 280.14 g mol^{-1}). **Fig. S9** shows the mass response obtained in the two media, measured under the same conditions as in **Fig. 3d**. In the LiTFSI containing electrolyte (**Fig. S9b**), the Δm_{EQCM} is decreased by ~0.75 µg cm^{-2} comparing to that with $LiClO_4$ (**Fig. S9a**), and is lower than the theoretical faraday mass ($\Delta m_{Faraday}$). This large drop in experimental mass clearly implies the participation of anions in the overall charge storage mechanism as well as its presence in the Inner Helmholtz Plane, IHP. *Ac*-electrogravimetry was equally performed with 1M LiTFSI in PC electrolyte (shown for measurements at 2.3 V *vs* Li/Li^+ in **Fig. S10**), and the data analysed with the same set of species as in the $LiClO_4$ containing electrolyte. This analysis unambiguously confirms the presence of $TFSI^-$ anions in the EDL despite their heavier molar weight and larger size.

Next, we interrogate the effect of solvent polarity over the structuration of EDL while keeping the same $LiClO_4$ salt. More specifically, we chose DMC and a binary mixture of EC:DMC (1:1 as opposed to PC. It is noted that dipole moments of PC, EC and DMC molecules decrease in the same order (5.6, 5.3 and 0.35 D, respectively).[43] The mass responses of Li_xMoO_3 thin films in the three different electrolytes are shown in **Fig. 5a** (*i.e.,* 1M $LiClO_4$ in DMC, EC:DMC and PC). The disparity between the Δm_{EQCM} and $\Delta m_{Faraday}$ values has a distinct upward trend as the polarity of the solvent increases (**Fig. 5b**). This can be explained simply by the fact that the higher the dipole moment of the solvent, the more energy it takes for Li^+ to break off its solvation shell when it reaches the Outer Helmholtz Plane (OHP), implying that Li^+ in PC and EC:DMC retains some of its solvation shell, whereas Li^+ is transferred in its bare form in DMC. Thus, the increase in the Δm_{EQCM}-$\Delta m_{Faraday}$ values indicates an increase in the contribution of the solvated Li^+ species (**Fig. 5b**) in accordance with the solvation energies reported for the same solvents.[43]

This hypothesis is further confirmed by the *ac*-electrogravimetric analyses, where the set of species used to fit the DMC electrolyte data contains only bare Li^+ as the charged species (**Fig. S11**), in contrast to the PC-containing electrolyte. In DMC, a slight contribution from the free solvent molecules is observed, rather than the solvent molecules in the solvation shell of the Li^+, further confirming the ease of desolvation in DMC. The result is confirmed with both 1M $LiClO_4$ and 1M LiTFSI salts in presence of DMC solvents (**Fig. S11** and **12**).

Besides, one can also observe the total suppression of anion response in charge compensation as the semi-circle usually attributed to ClO_4^- has disappeared (**Fig. S11**). This could simply correspond to an absence of the usual opposite flux to bare/solvated Li^+ ions' interfacial transfer recorded in the PC containing electrolyte. Meaning that in the DMC electrolyte, ClO_4^- anions are still at the interface and unable to leave the EDL after polarization of Li_xMoO_3 electrode. The most plausible hypothesis elucidating this phenomenon is the formation of Contact Ion Pairs (CIPs) and aggregates. This can be further explained by the displacement of solvent molecules in the first solvation shell of Li^+ by anions, forming cation-anion CIPs[44], thus preventing ClO_4^- from leaving the interface or participating to the charge-compensation process (**Fig. 6**).[45] The same behavior has been observed when changing the anion from ClO_4^- to $TFSI^-$, *i.e.,* 1M LiTFSI in DMC electrolyte (**Fig. S12**). This can be interpreted as "a less mobile interface" when DMC is used as a solvent, compared with PC. These experimental results, observed in DMC but not in PC, are in agreement with the trends in their dielectric constants, since ion pair formation is less pronounced in highly polar solvents, supported by the theoretical studies.[46]

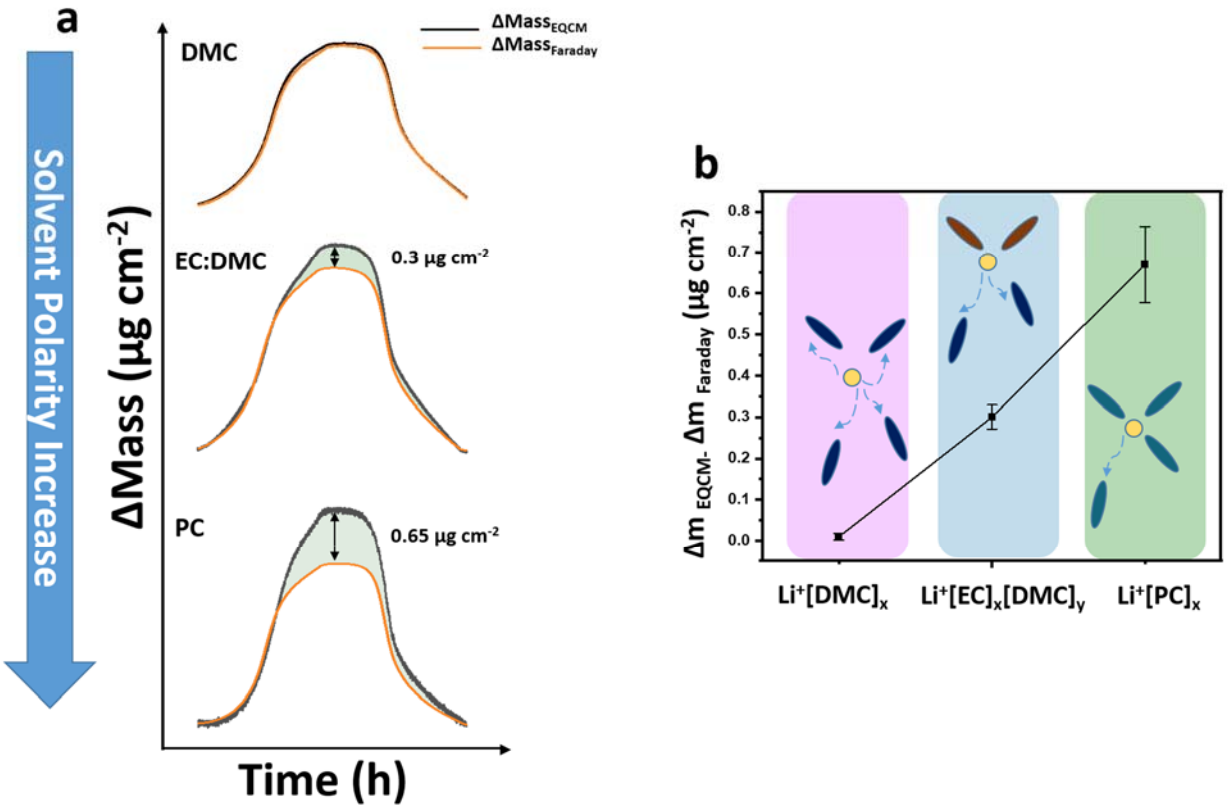

Figure 5. a) Comparison between Faraday masses (calculated assuming solely Li^+ participating in charge compensation) and measured EQCM masses in different solvents (DMC (upper), EC:DMC (middle) and PC (lower)) and b) tendency of the difference between both masses (Δm_{EQCM}-$\Delta m_{Faraday}$) following the binding energy of solvated Li^+ species in each solvent.[43] EQCM measurements were performed at 1 mV s^{-1}, under the same conditions as in **Fig. 2** and **3**. The 15th cycle of each measurement is shown.

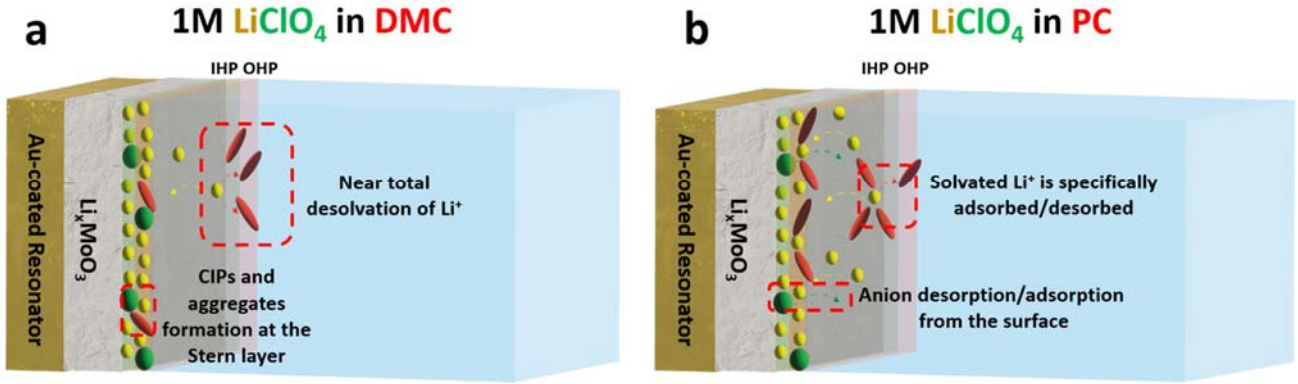

Figure 6. Schematic illustration of the EDL structure evolution related to solvent polarity. a) 1M $LiClO_4$ in DMC and b) 1M $LiClO_4$ in PC.

Conclusions

EDL formation is an omnipresent phenomenon occurring in all types of electrochemical energy storage devices and its chemical structuration and evolution through electrode polarization remain crucial for the device's general behavior. To enrich our knowledge of the EDL we have reported its chemical-physical structuration as the surface of an electrodeposited α-MoO_3 electrode. We highlighted the benefits of advanced *ac*-electrogravimetry for probing the dynamic of the double layer structuring in both qualitative and quantitate ways, using several electrolyte combinations. We revealed the presence of an anionic response through (electro)adsorption/desorption in electrolytes with highly polar solvents such as PC or EC:DMC mixtures, as opposed to less polar solvent in the form of DMC where the probability of CIPs and aggregates formation is higher (**Fig. 6a**). More importantly, we noticed a repeatable trend in mass difference between EQCM and theoretical masses, namely an increase that scales with the solvent polarity. This demonstrates in a straightforward manner how classical EQCM, in addition to the complementary *ac*-electrogravimetry, can be a powerful tool to accurately determine how Li^+ solvation shell can evolve at electrolyte electrode interface. We thus hope that this advanced analytical approach will rapidly be adopted by the battery community and scientists studying energy related redox and capacitive processes.

Experimental section:

Electrodeposition of α-MoO_3. Thin films of MoO_3 were deposited directly onto gold patterned AT-cut 9MHz quartz resonators (Bio-Logic) *via* chronoamperometry using a protocol adapted from Ref.[29] The electrolyte for electrodeposition process is consisted of 0.2M Na_2MoO_4 (Sigma-Aldrich, ≥98%) acidified down to pH=4 by concentrated H_2SO_4 (97%, Sigma-Aldrich) with deionized water (resistivity of 18.2 MΩ cm, purified by using a Milli-Q filtering system (Millipore)). A cathodic potential of -1V *vs* Hg/Hg_2SO_4 (K_2SO_4 (sat'd)) was applied through the gold coated QCM resonator (0.196 cm^2) that acted as the working electrode, a Pt mesh was used as counter electrode. A loading of 30 ±5 $\mu g.cm^{-2}$ was achieved after 60 seconds of electrodeposition (**Fig. S1**). The QCM electrode was then rinsed with deionized water to remove excess salt and was subsequently heated up to 300 °C under air for 3h to obtain crystalline α-MoO_3 structure (see XRD pattern in **Fig. 1b**).

Physical characterisations. The morphological aspect of the electrodeposited MoO_3 films was examined under a field emission gun scanning electron microscope (FEG-SEM) (Ultra55, Zeiss) operating at 5 kV. HRTEM sample preparation was done through electrodeposition of the samples on a 2x2cm ITO substrate (purchased from Saint Gobain, France) followed by a heat treatment at 300°C for 3h. The α-MoO_3 was then gently scrapped off the surface, whereas the lithiated sample was made by reducing the α-MoO_3 loaded ITO substrate *vs* Lithium metal down to 1.5V *vs* Li/Li^+. HRTEM images and SAED patterns were collected with a Titan Themis Z transmission electron microscope operated at 200 kV. *In situ* XRD during electrochemical cycling was carried out using a laboratory X-ray diffractometer (BRUKER D8 Advance) equipped with a Cu K_α radiation source ($\lambda_{K\alpha1}$=1.54056Å, $\lambda_{K\alpha2}$=1.54439Å) and a Lynxeye XE detector (**Fig. 1e**). The sample was a 80*wt*% and 20*wt*% mixture of commercial MoO_3 powder (Sigma Aldrich, 99.5%) and carbon black (Alfa Aesar, 99%) (**Fig. 1e** and **Fig. S7**). The crystallite size of the thin film was estimated using Scherer equation (XRD pattern in **Fig. 1b**), (*i.e.,* $\mathcal{T} = 0.89\lambda/\beta\cos\theta$), where λ is the wavelength of X-ray radiation, $\mathcal{T}$ the average crystallite size, θ the diffraction angle, and β is the full width at the half maximum (FWHM).[30]

Electrochemical and electrogravimetric characterization. The gold-patterned 9MHz QCM resonators modified with the MoO_3 thin films were mounted in an airtight EQCM cell developed in our previous work, as described in Ref[23]. The cell is mounted in an Ar-filled glove-box and the measurements were conducted outside the glove-box. The EQCM-R measurements were performed using a Biologic SP200 workstation coupled with a commercial SEIKO QCM922A microbalance which permitted the resonance frequency (f) along with the motional resistance (R_m) to be monitored during electrochemical cycling. MoO_3 coated QCMs act as working electrode and metallic lithium acts as both reference and counter electrodes. The electrolyte concentration (1 mol L^{-1}) was kept constant, using 2 different salts (Lithium perchlorate ($LiClO_4$), Lithium bis(trifluoromethanesulfonyl)imide (LiTFSI)) in combination with 3 different solvents (PC, EC:DMC (1:1 mol) and DMC). The cell was cycled using CV for at least 15 cycles to stabilize the film, the frequency response was translated into mass change with Sauerbrey interpretation,[40] from the 20th cycle onwards. The gravimetric regime conditions were fulfilled (high $\Delta f/\Delta R_m$ and $|\Delta W| << |\Delta f|$), indicating an electroacoustically thin, rigid and flat surface film formation with good adhesion to the substrate, the Sauerbrey equation[40] was therefore applicable:

$$\Delta m = -\frac{A\sqrt{\rho_q \mu_q}}{2f_0^2}\,\Delta f = -C_f \Delta f$$ Equation 1

where A is the piezoelectrically active area (0.2 cm²), ρ_q the density of quartz (2.648 g.cm^{-3}) and μ_q is the shear modulus of the quartz crystal (2.947 10^{11} g.cm^{-1}.s^{-2}), C_f is the sensitivity coefficient/calibration constant which is 1.23 ng.Hz^{-1} ± 0.03 and determined by Ag electrodeposition (more details in Support Information File, Part I). The mass per electron estimation is done by using the slope of the Δm *vs* ΔQ plots (**Fig. 3**) where $M.P.E. = \frac{nF\Delta m}{\Delta Q}$, with F is the Faraday's constant and *n* is the number of electrons transferred.

A four-channel frequency response analyzer (FRA, Solartron 1254) and a lab-made potentiostat (SOTELEM-PGSTAT) were utilized for ac-electrogravimetry measurements.[27,28] The sample was placed in the previously mentioned airtight EQCM cell and pre-treated with 15 to 20 CV cycles beforehand. The EQCM was carried out in a dynamic regime, with the α-MoO_3-loaded working electrode polarized at multiple potentials to which a small amplitude sinusoidal potential perturbation (80 mV) was superimposed. The frequency range was between 63 kHz and 1 mHz. The mass change, Δm, of the working electrode was measured at the same time as the electrochemical system's ac response, ΔI. At a particular voltage and frequency modulation, f (pulsation ω = 2 πf), the experimental electrogravimetric TF (Δ*m*/Δ*E*(ω)) and the electrochemical transfer function (TF) (Δ*E*/Δ*I*(ω)) were obtained concurrently. The latter was presented as the charge/potential TF, Δ*q*/Δ*E*(ω), which is more convenient to separate the different species' participation in the charge compensation process. The theoretical equations in the model presented in Part III of the Supporting Information File are used to fit the experimental TFs. Further details of the methodology can be found in previous works.[25–28]

Associated Content

Supporting Information. α-MoO_3 thin film synthesis details monitored by EQCM-R, validation of the gravimetric sensing conditions for the electrogravimetric studies, theoretical background for *ac*-electrogravimetry measurements, and additional *ac*-electrogravimerty data measured in 1M LiX (X = ClO_4, TFSI) in PC and LiX (X = ClO_4, TFSI) in DMC.

Author Information

Corresponding Authors

* Ozlem Sel - Chimie du Solide et de l'Energie, UMR 8260, Collège de France, 11 Place Marcelin Berthelot, 75231 Paris Cedex 05, France; orcid.org/0000-0002-8501-4561; E-mail: ozlem.sel@college-de-france.fr

* Jean-Marie Tarascon - Chimie du Solide et de l'Energie, UMR 8260, Collège de France, 11 Place Marcelin Berthelot, 75231 Paris Cedex 05, France; orcid.org/0000-0002-7059- 6845; E-mail: jean-marie.tarascon@college-de-france.fr

Acknowledgements

EB, OS and JMT acknowledges the "Sorbonne Université - Programme doctoral Génie des Procédés" for the PhD scholarship. Access to TEM facilities was granted by the Advance Imaging Core Facility of Skoltech.

Notes

The authors declare no competing financial interest.

References

(1) Armand, M.; Tarascon, J.-M. Building Better Batteries. *Nature* **2008**, *451*, 652–657. https://doi.org/10.1038/451652a.
(2) Winter, M.; Brodd, R. J. What Are Batteries, Fuel Cells, and Supercapacitors? *Chem. Rev.* **2004**, *104*, 4245–4270. https://doi.org/10.1021/cr020730k.
(3) Simon, P.; Gogotsi, Y. Materials for Electrochemical Capacitors. In *Nanoscience and technology: a collection of reviews from Nature journals*; World Scientific, **2010**; pp 320–329.
(4) Waegele, M. M.; Gunathunge, C. M.; Li, J.; Li, X. How Cations Affect the Electric Double Layer and the Rates and Selectivity of Electrocatalytic Processes. *J. Chem. Phys.* **2019**, *151*, 160902. https://doi.org/10.1063/1.5124878.
(5) Ji, X. A Paradigm of Storage Batteries. *Energy Environ. Sci.* **2019**, *12*, 3203–3224. https://doi.org/10.1039/C9EE02356A.
(6) Lück, J.; Latz, A. Modeling of the Electrochemical Double Layer and Its Impact on Intercalation Reactions. *Phys. Chem. Chem. Phys.* **2018**, *20*, 27804–27821. https://doi.org/10.1039/C8CP05113E.
(7) Bai, P.; Bazant, M. Z. Charge Transfer Kinetics at the Solid–Solid Interface in Porous Electrodes. *Nat. Commun.* **2014**, *5*, 3585. https://doi.org/10.1038/ncomms4585.
(8) Magnussen, O. M.; Groß, A. Toward an Atomic-Scale Understanding of Electrochemical Interface Structure and Dynamics. *J. Am. Chem. Soc.* **2019**, *141*, 4777–4790. https://doi.org/10.1021/jacs.8b13188.

(9) Ding, S.-Y.; Yi, J.; Li, J.-F.; Ren, B.; Wu, D.-Y.; Panneerselvam, R.; Tian, Z.-Q. Nanostructure-Based Plasmon-Enhanced Raman Spectroscopy for Surface Analysis of Materials. *Nat. Rev. Mater.* **2016**, *1*, 1–16. https://doi.org/10.1038/natrevmats.2016.21.
(10) Wang, X.; Huang, S.-C.; Huang, T.-X.; Su, H.-S.; Zhong, J.-H.; Zeng, Z.-C.; Li, M.-H.; Ren, B. Tip-Enhanced Raman Spectroscopy for Surfaces and Interfaces. *Chem. Soc. Rev.* **2017**, *46*, 4020–4041. https://doi.org/10.1039/C7CS00206H.
(11) Iwasita, T.; Nart, F. C. In Situ Infrared Spectroscopy at Electrochemical Interfaces. *Prog. Surf. Sci.* **1997**, *55*, 271–340. https://doi.org/10.1016/S0079-6816(97)00032-4.
(12) Kötz, E. R.; Neff, H.; Müller, K. A UPS, XPS and Work Function Study of Emersed Silver, Platinum and Gold Electrodes. *J. Electroanal. Chem. Interfacial Electrochem.* **1986**, *215*, 331–344. https://doi.org/10.1016/0022-0728(86)87026-7.
(13) Kolb, D. M.; Michaelis, R. Influence of the Surface Electric Field on the Electronic States of an Adsorbate. *J. Electroanal. Chem. Interfacial Electrochem.* **1990**, *284*, 507–510. https://doi.org/10.1016/0022-0728(90)85055-A.
(14) Zhang, X.; Zhong, Y.-X.; Yan, J.-W.; Su, Y.-Z.; Zhang, M.; Mao, B.-W. Probing Double Layer Structures of Au (111)–BMIPF6 Ionic Liquid Interfaces from Potential-Dependent AFM Force Curves. *Chem. Commun.* **2011**, *48*, 582–584. https://doi.org/10.1039/C1CC15463J.
(15) Zhong, Y.-X.; Yan, J.-W.; Li, M.-G.; Zhang, X.; He, D.-W.; Mao, B.-W. Resolving Fine Structures of the Electric Double Layer of Electrochemical Interfaces in Ionic Liquids with an AFM Tip Modification Strategy. *J. Am. Chem. Soc.* **2014**, *136*, 14682–14685. https://doi.org/10.1021/ja508222m.
(16) Mozhzhukhina, N.; Flores, E.; Lundström, R.; Nyström, V.; Kitz, P. G.; Edström, K.; Berg, E. J. Direct Operando Observation of Double Layer Charging and Early Solid Electrolyte Interphase Formation in Li-Ion Battery Electrolytes. *J. Phys. Chem. Lett.* **2020**, *11*, 4119–4123. https://doi.org/10.1021/acs.jpclett.0c01089.
(17) Lemaire, P. Exploring Interface Mechanisms in Metal-Ion Batteries via Advanced EQCM. phdthesis, Sorbonne Université, **2020**. https://doi.org/10/document.
(18) Shpigel, N.; Levi, M. D.; Aurbach, D. EQCM-D Technique for Complex Mechanical Characterization of Energy Storage Electrodes: Background and Practical Guide. *Energy Storage Mater.* **2019**, *21*, 399–413. https://doi.org/10.1016/j.ensm.2019.05.026.
(19) Tadmor, R.; Hernández-Zapata, E.; Chen, N.; Pincus, P.; Israelachvili, J. N. Debye Length and Double-Layer Forces in Polyelectrolyte Solutions. *Macromolecules* **2002**, *35*, 2380–2388. https://doi.org/10.1021/ma011893y.
(20) Levi, M. D.; Shpigel, N.; Sigalov, S.; Dargel, V.; Daikhin, L.; Aurbach, D. In Situ Porous Structure Characterization of Electrodes for Energy Storage and Conversion by EQCM-D: A Review. *Electrochimica Acta* **2017**, *232*, 271–284. https://doi.org/10.1016/j.electacta.2017.02.149.
(21) Kitz, P.; Lacey, M.; Novák, P.; Berg, E. Operando Investigation of the Solid Electrolyte Interphase Mechanical and Transport Properties Formed from Vinylene Carbonate and Fluoroethylene Carbonate. *J. Power Sources* **2020**, *477*, 228567. https://doi.org/10.1016/j.jpowsour.2020.228567.
(22) Shpigel, N.; Levi, M. D.; Sigalov, S.; Girshevitz, O.; Aurbach, D.; Daikhin, L.; Pikma, P.; Marandi, M.; Jänes, A.; Lust, E. In Situ Hydrodynamic Spectroscopy for Structure Characterization of Porous Energy Storage Electrodes. *Nat. Mater.* **2016**, *15*, 570–575.
(23) Lemaire, P.; Dargon, T.; Alves Dalla Corte, D.; Sel, O.; Perrot, H.; Tarascon, J.-M. Making Advanced Electrogravimetry as an Affordable Analytical Tool for Battery Interface Characterization. *Anal. Chem.* **2020**, *92*, 13803–13812. https://doi.org/10.1021/acs.analchem.0c02233.
(24) Lemaire, P.; Serva, A.; Salanne, M.; Rousse, G.; Perrot, H.; Sel, O.; Tarascon, J.-M. Probing the Electrode–Electrolyte Interface of a Model K-Ion Battery Electrode–The Origin of Rate Capability Discrepancy between Aqueous and Non-Aqueous Electrolytes. *ACS Appl. Mater. Interfaces* **2022**, *14*, 20835–20847. https://doi.org/10.1021/acsami.1c24111.
(25) Gao, W.; Debiemme-Chouvy, C.; Lahcini, M.; Perrot, H.; Sel, O. Tuning Charge Storage Properties of Supercapacitive Electrodes Evidenced by In Situ Gravimetric and Viscoelastic Explorations. *Anal. Chem.* **2019**, *91*, 2885–2893. https://doi.org/10.1021/acs.analchem.8b04886.

(26) Lemaire, P.; Sel, O.; Alves Dalla Corte, D.; Iadecola, A.; Perrot, H.; Tarascon, J.-M. Elucidating the Origin of the Electrochemical Capacity in a Proton-Based Battery H x IrO4 via Advanced Electrogravimetry. *ACS Appl. Mater. Interfaces* **2019**, *12*, 4510–4519.
(27) Gabrielli, C.; Garcia-Jareño, J. J.; Keddam, M.; Perrot, H.; Vicente, F. Ac-Electrogravimetry Study of Electroactive Thin Films. II. Application to Polypyrrole. *J. Phys. Chem. B* **2002**, *106*, 3192–3201. https://doi.org/10.1021/jp013925p.
(28) Gabrielli, C.; García-Jareño, J. J.; Keddam, M.; Perrot, H.; Vicente, F. Ac-Electrogravimetry Study of Electroactive Thin Films. I. Application to Prussian Blue. *J. Phys. Chem. B* **2002**, *106*, 3182–3191. https://doi.org/10.1021/jp013924x.
(29) Yao, D. D.; Ou, J. Z.; Latham, K.; Zhuiykov, S.; O'Mullane, A. P.; Kalantar-zadeh, K. Electrodeposited α- and β-Phase MoO3 Films and Investigation of Their Gasochromic Properties. *Cryst. Growth Des.* **2012**, *12*, 1865–1870. https://doi.org/10.1021/cg201500b.
(30) Holzwarth, U.; Gibson, N. The Scherrer Equation versus the "Debye-Scherrer Equation." *Nat. Nanotechnol.* **2011**, *6*, 534–534. https://doi.org/10.1038/nnano.2011.145.
(31) Iriyama, Y.; Abe, T.; Inaba, M.; Ogumi, Z. Transmission Electron Microscopy (TEM) Analysis of Two-Phase Reaction in Electrochemical Lithium Insertion within α-MoO3. *Solid State Ion.* **2000**, *135*, 95–100. https://doi.org/10.1016/S0167-2738(00)00338-6.
(32) Kim, H.-S.; Cook, J. B.; Lin, H.; Ko, J. S.; Tolbert, S. H.; Ozolins, V.; Dunn, B. Oxygen Vacancies Enhance Pseudocapacitive Charge Storage Properties of MoO3−x. *Nat. Mater.* **2017**, *16*, 454–460. https://doi.org/10.1038/nmat4810.
(33) Tsumura, T.; Inagaki, M. Lithium Insertion/Extraction Reaction on Crystalline MoO3. *Solid State Ion.* **1997**, *104*, 183–189. https://doi.org/10.1016/S0167-2738(97)00418-9.
(34) Daikhin, L.; Gileadi, E.; Katz, G.; Tsionsky, V.; Urbakh, M.; Zagidulin, D. Influence of Roughness on the Admittance of the Quartz Crystal Microbalance Immersed in Liquids. *Anal. Chem.* **2002**, *74*, 554–561. https://doi.org/10.1021/ac0107610.
(35) Acharya, B.; Sidheswaran, M. A.; Yungk, R.; Krim, J. Quartz Crystal Microbalance Apparatus for Study of Viscous Liquids at High Temperatures. *Rev. Sci. Instrum.* **2017**, *88*, 025112. https://doi.org/10.1063/1.4976024.
(36) Cuenca, A.; Agrisuelas, J.; García-Jareño, J. J.; Vicente, F. Oscillatory Changes of the Heterogeneous Reactive Layer Detected with the Motional Resistance during the Galvanostatic Deposition of Copper in Sulfuric Solution. *Langmuir* **2015**, *31*, 12664–12673. https://doi.org/10.1021/acs.langmuir.5b03694.
(37) Gollas, B.; Bartlett, P. N.; Denuault, G. An Instrument for Simultaneous EQCM Impedance and SECM Measurements. *Anal. Chem.* **2000**, *72*, 349–356. https://doi.org/10.1021/ac990796o.
(38) Aurbach, D.; Zaban, A. The Application of EQCM to the Study of the Electrochemical Behavior of Propylene Carbonate Solutions. *J. Electroanal. Chem.* **1995**, *393*, 43–53. https://doi.org/10.1016/0022-0728(95)04014-F.
(39) Levi, M. D.; Daikhin, L.; Aurbach, D.; Presser, V. Quartz Crystal Microbalance with Dissipation Monitoring (EQCM-D) for in-Situ Studies of Electrodes for Supercapacitors and Batteries: A Mini-Review. *Electrochem. Commun.* **2016**, *67*, 16–21. https://doi.org/10.1016/j.elecom.2016.03.006.
(40) Sauerbrey, G. Verwendung von Schwingquarzen zur Wägung dünner Schichten und zur Mikrowägung. *Z. Für Phys.* **1959**, *155*, 206–222. https://doi.org/10.1007/BF01337937.
(41) Li, B.; Wang, Y.; Jiang, N.; An, L.; Song, J.; Zuo, Y.; Ning, F.; Shang, H.; Xia, D. Electrolytic-Anion-Redox Adsorption Pseudocapacitance in Nanosized Lithium-Free Transition Metal Oxides as Cathode Materials for Li-Ion Batteries. *Nano Energy* **2020**, *72*, 104727. https://doi.org/10.1016/j.nanoen.2020.104727.
(42) Waegele, M. M.; Gunathunge, C. M.; Li, J.; Li, X. How Cations Affect the Electric Double Layer and the Rates and Selectivity of Electrocatalytic Processes. *J. Chem. Phys.* **2019**, *151*, 160902. https://doi.org/10.1063/1.5124878.
(43) Skarmoutsos, I.; Ponnuchamy, V.; Vetere, V.; Mossa, S. Li+ Solvation in Pure, Binary, and Ternary Mixtures of Organic Carbonate Electrolytes. *J. Phys. Chem. C* **2015**, *119*, 4502–4515. https://doi.org/10.1021/jp511132c.

(44) Forero-Saboya, J. D.; Marchante, E.; Araujo, R. B.; Monti, D.; Johansson, P.; Ponrouch, A. Cation Solvation and Physicochemical Properties of Ca Battery Electrolytes. *J. Phys. Chem. C* **2019**, *123*, 29524–29532. https://doi.org/10.1021/acs.jpcc.9b07308.
(45) Yu, Z.; Balsara, N. P.; Borodin, O.; Gewirth, A. A.; Hahn, N. T.; Maginn, E. J.; Persson, K. A.; Srinivasan, V.; Toney, M. F.; Xu, K.; Zavadil, K. R.; Curtiss, L. A.; Cheng, L. Beyond Local Solvation Structure: Nanometric Aggregates in Battery Electrolytes and Their Effect on Electrolyte Properties. *ACS Energy Lett.* **2022**, *7*, 461–470. https://doi.org/10.1021/acsenergylett.1c02391.
(46) Ponnuchamy, V.; Mossa, S.; Skarmoutsos, I. Solvent and Salt Effect on Lithium Ion Solvation and Contact Ion Pair Formation in Organic Carbonates: A Quantum Chemical Perspective. *J. Phys. Chem. C* **2018**, *122*, 25930–25939. https://doi.org/10.1021/acs.jpcc.8b09892.